Two Warm, Low-density Sub-Jovian Planets Orbiting Bright Stars in *K2* Campaigns 13 and 14

Liang Yu[1], Joseph E. Rodriguez[2], Jason D. Eastman[2], Ian J. M. Crossfield[1], Avi Shporer[1], B. Scott Gaudi[3],
Jennifer Burt[1], Benjamin J. Fulton[4,17], Evan Sinukoff[5,6], Andrew W. Howard[5], Howard Isaacson[7],
Molly R. Kosiarek[8,18], David R. Ciardi[9], Joshua E. Schlieder[10], Kaloyan Penev[11], Andrew Vanderburg[12,19],
Keivan G. Stassun[13], Allyson Bieryla[2], R. Paul Butler[14], Perry Berlind[2], Michael L. Calkins[2], Gilbert A. Esquerdo[2],
David W. Latham[2], Gabriel Murawski[15], Daniel J. Stevens[3], Erik A. Petigura[5,20], Laura Kreidberg[2], and
Makennah Bristow[16]
[1] Department of Physics, and Kavli Institute for Astrophysics and Space Research, Massachusetts Institute of Technology, Cambridge, MA 02139, USA
[2] Harvard-Smithsonian Center for Astrophysics, Cambridge, MA 02138, USA
[3] Department of Astronomy, The Ohio State University, Columbus, OH 43210, USA
[4] Department of Geology and Planetary Sciences, California Institute of Technology, Pasadena, CA 91125, USA
[5] Cahill Center for Astrophysics, California Institute of Technology, Pasadena, CA 91125, USA
[6] Institute for Astronomy, University of Hawai'i at Mānoa, Honolulu, HI 96822, USA
[7] Department of Astronomy, University of California, Berkeley, CA 94720, USA
[8] Department of Astronomy and Astrophysics, University of California, Santa Cruz, CA 95064, USA
[9] NASA Exoplanet Science Institute, California Institute of Technology, Pasadena, CA 91125, USA
[10] NASA Goddard Space Flight Center, 8800 Greenbelt Road, Greenbelt, MD 20771, USA
[11] Department of Physics, The University of Texas at Dallas, 800 West Campbell Road, Richardson, TX 75080, USA
[12] Department of Astronomy, The University of Texas at Austin, Austin, TX 78712, USA
[13] Vanderbilt University, Department of Physics and Astronomy, 6301 Stevenson Center Lane, Nashville, TN 37235, USA
[14] Department of Terrestrial Magnetism, The Carnegie Institution for Science, NW Washington, DC 20015, USA
[15] Gabriel Murawski Private Observatory (SOTES), Suwałki, Poland
[16] Department of Physics, University of North Carolina at Asheville, Asheville, NC 28804, USA

Abstract

We report the discovery of two planets transiting the bright stars HD 89345 (EPIC 248777106, $V = 9.376$, $K = 7.721$) in *K2* Campaign 14 and HD 286123 (EPIC 247098361, $V = 9.822$, $K = 8.434$) in *K2* Campaign 13. Both stars are G-type stars, one of which is at or near the end of its main-sequence lifetime, and the other is just over halfway through its main-sequence lifetime. HD 89345 hosts a warm sub-Saturn (0.66 R_J, 0.11 M_J, $T_{eq} = 1100$ K) in an 11.81 day orbit. The planet is similar in size to WASP-107b, which falls in the transition region between ice giants and gas giants. HD 286123 hosts a Jupiter-sized, low-mass planet (1.06 R_J, 0.39 M_J, $T_{eq} = 1000$ K) in an 11.17 day, mildly eccentric orbit, with $e = 0.255 \pm 0.035$. Given that they orbit relatively evolved main-sequence stars and have orbital periods longer than 10 days, these planets are interesting candidates for studies of gas planet evolution, migration, and (potentially) reinflation. Both planets have spent their entire lifetimes near the proposed stellar irradiation threshold at which giant planets become inflated, and neither shows any sign of radius inflation. They probe the regime where inflation begins to become noticeable and are valuable in constraining planet inflation models. In addition, the brightness of the host stars, combined with large atmospheric scale heights of the planets, makes these two systems favorable targets for transit spectroscopy to study their atmospheres and perhaps provide insight into the physical mechanisms that lead to inflated hot Jupiters.

Key words: planetary systems – stars: individual (HD 89345, HD 286123) – techniques: photometric – techniques: spectroscopic

1. Introduction

Giant planets have historically been an important class of transiting exoplanets, and many questions have been raised about their formation and evolution. The discovery of the first hot Jupiters immediately upended all existing giant planet formation models, which were based on observations of the solar system. One of the most pressing open questions is how hot Jupiters, or Jupiter-mass planets orbiting at only a few percent of an astronomical unit from their host stars, are able to reach such short orbital periods. Although in situ formation has been considered as a possibility (e.g., Bodenheimer et al. 2000;

Batygin et al. 2016), hot Jupiters are most commonly thought to have formed at large radial distances and subsequently migrated inward to their present orbits. There have been several theories attempting to explain hot Jupiter migration. Some invoke interactions with a planetary or stellar companion: the gas giant planet is first injected into an eccentric orbit, which then undergoes tidal circularization (e.g., Rasio & Ford 1996; Fabrycky & Tremaine 2007). Other theories suggest processes where the gas giant planet gradually moves inward by interacting with the protoplanetary disk, during which the orbit is kept circular (e.g., Lin et al. 1996; Alibert et al. 2005). The two theories predict different orbital eccentricities and stellar obliquities as the planet migrates inward, yet it appears that stellar obliquities in hot Jupiter systems may be erased by tides raised by the planet on the star (e.g., Schlaufman 2010; Winn et al. 2010). We would then expect warm Jupiters—gas giants
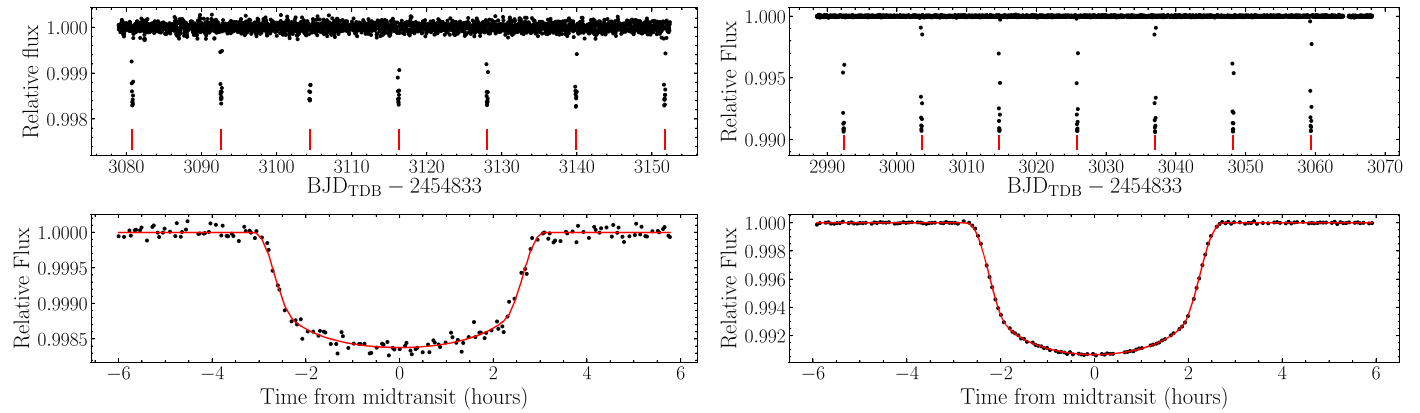
Figure 1. Left: calibrated *K2* photometry for HD 89345 (top), with vertical ticks indicating the locations of the transits, and phase-folded photometry and best-fit light curve model (bottom). Right: same, but for HD 286123.

with orbital periods of 10 days or longer—which experience weaker tidal effects, to have retained the obliquity they had when emplaced in their current orbits. In reality, however, the interpretation is not that simple, as Mazeh et al. (2015) found that warm Jupiters seem to be showing effects of tidal realignment even at orbital distances where tidal effects should be negligible.

Another long-standing mystery is the anomalously large radii of "inflated" close-in giant planets. Many of the known transiting hot Jupiters have radii larger than expected by standard models of giant planets (see, e.g., Burrows et al. 1997; Bodenheimer et al. 2001; Guillot & Showman 2002). Dozens of inflated hot Jupiters with radii $>1.2 R_J$ have been observed to orbit stars several gigayears old (Guillot & Gautier 2014). Although very young planets (<10 Myr) are expected to have radii this large, it is unclear how such inflated planets can exist around mature main-sequence and even evolved stars (e.g., Grunblatt et al. 2017).

Various mechanisms have been proposed to explain the large radii of hot Jupiters. Following Lopez & Fortney (2016), the suggested mechanisms for inflating gas giants can be divided into two categories: in class I mechanisms, the stellar irradiation incident on a planet is transported into the planet's deep interior, driving adiabatic heating of the planet and causing it to expand (e.g., Arras & Socrates 2010; Batygin & Stevenson 2010); in class II mechanisms, the inflationary mechanism simply acts to slow radiative cooling through the atmosphere, allowing a planet to retain its initial heat and inflated radius from formation (delayed contraction, e.g., Burrows et al. 2007). The observation that the radii of giant planets increase with incident stellar irradiation hints that giant planet inflation is intimately linked to irradiation (Burrows et al. 2000; Bodenheimer et al. 2001; Lopez & Fortney 2016). We can distinguish between these two classes of models by studying warm Jupiters around stars that have recently evolved off the main sequence (e.g., Shporer et al. 2017; Smith et al. 2017). The irradiation levels experienced by warm Jupiters around main-sequence stars are not high enough to cause inflation, but as their host stars move up the subgiant and red-giant branches, they will experience enormous increases in their irradiation levels. If class I mechanisms are responsible for giant planet inflation, then warm Jupiters should inflate in response to the increased irradiation (Assef et al. 2009; Spiegel & Madhusudhan 2012; Hartman et al. 2016). On the other hand, an exclusively noninflated population of warm Jupiters

around evolved stars would favor class II mechanisms (Lopez & Fortney 2016).

Finally, we have yet to even understand the formation mechanism of giant planets. The positive correlation between the fraction of stars with short-period giant planets and stellar metallicity hints that planets form through core accretion (e.g., Santos et al. 2004; Johnson et al. 2010). In the core accretion scenario, a rocky core forms through the coagulation of planetesimals; when the mass of the gaseous envelope relative to the solid core mass reaches a critical ratio, rapid gas accretion occurs and a giant planet is formed (e.g., Pollack et al. 1996). Gas accretion is expected to start in the mass regime between Neptune and Saturn (Mordasini et al. 2015), the transition zone between ice giants and gas giants. Yet this regime is not very well understood given the small number of known planets that fall within this mass range. In particular, the core accretion model struggles to explain why ice giants do not undergo the runaway gas accretion that would have turned them into gas giants (Helled & Bodenheimer 2014).

In this paper, we present the discovery of two exoplanets observed by *K2*, which are pertinent to the problems described above: one sub-Saturn transiting a bright star HD 89345 (EPIC 248777106), and a warm Saturn orbiting a similarly bright star HD 286123 (EPIC 247098361), with both stars well into or nearing the ends of their main-sequence lifetimes. Despite their large radii, both planets have low masses, which make them promising targets for atmospheric characterization. They are also interesting additions to the currently available set of giant planets to study radius inflation, which consists primarily of Jupiter-massed objects. We describe our discovery and observations in Section 2, our derivation of stellar and planetary parameters in Sections 3 and 4, and potential implications for giant planet migration, inflation, and formation theories in Section 5.

2. Observations

HD 286123 was proposed as a *K2* target in Campaign 13 (C13) in four programs: GO13071 (PI Charbonneau), GO13122 (PI Howard), GO13024 (PI Cochran), and GO13903 (GO Office). HD 89345 was proposed as a target in Campaign 14 (C14) in five programs: GO14010 (PI Lund), GO14009 (PI Charbonneau), GO14028 (PI Cochran), GO14021 (PI Howard) and GO14901 (GO Office). C13 was observed from 2017 March 08 to May 27, and C14 was observed from 2017 June 01 to August 19. HD 89345 and HD

Table 1
Stellar Parameters of HD 89345 and HD 286123 from the Literature and
Spectroscopy

Parameter	HD 89345	HD 286123	Source
Identifying Information			
α_{J2000} R.A. (hh: mm:ss)	10:18:41.06	04:55:03.96	
δ_{J2000} Decl. (dd:mm:ss)	10:07:44.5	18:39:16.33	
Other identifiers	TYC 840-840-1	TYC 1284-745-1	
	2MASS J10184106 +1007445	2MASS J04550395 +1839164	
	EPIC 248777106	EPIC 247098361	
	K2-234	K2-232	
K2 campaign	14	13	
Photometric Properties			
B (mag)	10.148 ± 0.039	10.520 ± 0.051	1
V (mag)	9.376 ± 0.028	9.822 ± 0.038	1
J (mag)	8.091 ± 0.020	8.739 ± 0.030	2
H (mag)	7.766 ± 0.040	8.480 ± 0.018	2
Ks (mag)	7.721 ± 0.018	8.434 ± 0.017	2
W1 (mag)	7.763 ± 0.028	8.380 ± 0.024	3
W2 (mag)	7.759 ± 0.020	8.419 ± 0.019	3
W3 (mag)	7.729 ± 0.019	8.391 ± 0.027	3
Spectroscopic and Derived Properties			
Spectral Type	G5V–G6V	F9V–G0V	4
μ_α (mas yr^{-1})	5.348 ± 0.079	62.064 ± 0.077	5
μ_δ (mas yr^{-1})	-42.449 ± 0.071	-48.245 ± 0.051	5
Parallax (mas)	7.528 ± 0.046	7.621 ± 0.044	5
Barycentric RV (km s^{-1})	2.4 ± 0.1	22.4 ± 0.1	TRES; this paper
$v \sin i$ (km s^{-1})	3 ± 1	3 ± 1	APF; this paper
Space motion (U^a, V, W) (km s^{-1})	$(21.5 \pm 0.1, -9.8 \pm 0.1, 1.5 \pm 0.1)$	$(-14.9 \pm 0.1, -34.5 \pm 0.3, 13.5 \pm 0.1)$	this paper

Note.
[a] Positive *U* is in the direction of the Galactic center.
References. (1) Høg et al. (2000); (2) Skrutskie et al. (2006); (3) Wright et al. (2010), Cutri et al. (2014); (4) Pecaut & Mamajek (2013); (5) Gaia Collaboration et al. (2016, 2018).

286123's photometric and spectroscopic properties are given in Table 1.

2.1. K2 Photometry

We converted the processed *K2* target pixel files into light curves using an approach identical to that described in Crossfield et al. (2015). In brief, we computed the raw photometry by summing the flux within a soft-edged circular aperture centered around the target star, and used the publicly available `k2phot` photometry code[21] to model out the time- and roll-dependent variations with a Gaussian process. We then used the publicly available `TERRA` algorithm[22] (Petigura et al. 2013a, 2013b) to search for transit-like events and manually examined diagnostic plots for all signals with S/N $\geqslant$ 10. `TERRA` identified a planet candidate orbiting HD 89345 with

---

[21] https://github.com/petigura/k2phot
[22] https://github.com/petigura/terra

$P = 11.81$ days and S/N = 24 in Campaign 14, and another candidate orbiting HD 286123 with $P = 11.17$ days and S/N = 495 in Campaign 13.

After identifying the transits, we produced new light curves by simultaneously fitting the transits, the *K2* roll systematics, and long-timescale stellar/instrumental variability. Reprocessing the *K2* light curves in this way prevents the shape of the transits from being biased by the removal of *K2* systematics. We used light curves and systematics corrections derived using the method of Vanderburg & Johnson (2014) as initial guesses for our simultaneous fits, which we then performed following Vanderburg et al. (2016). Throughout the rest of this paper, we use these simultaneously fit light curves in our analysis and our plots. Figure 1 shows the flattened[23] and detrended light curves of HD 89345 and HD 286123.

2.2. Ground-based Follow-up

In this section, we present our ground-based photometric and spectroscopic observations used to confirm the planetary nature of HD 89345b and HD 286123b.

2.2.1. Spectroscopic Follow-up

We used the HIRES spectrograph (Vogt et al. 1994) at the W. M. Keck Observatory to measure high-resolution optical spectra of the two targets. Observations and data reduction followed the standard procedures of the California Planet Search (CPS; Howard et al. 2010). For both stars, the $0\farcs86 \times 14''$ "C2" decker was placed in front of the slit and the exposures were terminated once an exposure meter reached 10,000 counts, yielding a signal-to-noise ratio (S/N) of 45 per pixel at 550 nm. Additional spectra of HD 89345 were collected to measure precise radial velocities (RVs), by placing a cell of gaseous iodine in the converging beam of the telescope, just ahead of the spectrometer slit. The iodine cell is sealed and maintained at a constant temperature of $50.0 \pm 0.1°C$ to ensure that the iodine gas column density remains constant over decades. The iodine superimposes a rich forest of absorption lines on the stellar spectrum over the 500–620 nm region, thereby providing a wavelength calibration and proxy for the point-spread function (PSF) of the spectrometer. Once extracted, each spectrum of the iodine region is divided into ~700 chunks, each of which is 2 Å wide. Each chunk produces an independent measure of the wavelength, PSF, and Doppler shift, determined using the spectral synthesis technique described by Butler et al. (1996). The final reported Doppler velocity for a stellar spectrum is the weighted mean of the velocities of all the individual chunks. The final uncertainty of each velocity is the weighted average of all 700 chunk velocities. These iodine exposures were terminated after 50,000 counts (S/N = 100 per pixel), typically lasting 2 minutes. For both stars, a single iodine-free "template" spectrum with a higher S/N of 225 was also collected using the narrower "B3" decker ($0\farcs57 \times 14''$). RVs were measured using the standard CPS Doppler pipeline (Marcy & Butler 1992; Valenti et al. 1995; Butler et al. 1996; Howard et al. 2009). Each observed spectrum was forward modeled as the product of an RV-shifted iodine-free spectrum and a high-resolution/high-S/N iodine transmission spectrum

---

convolved with a PSF model. Typical internal RV uncertainties were $1.5\,\mathrm{m\,s^{-1}}$.

We obtained additional spectra for the two targets with the Tillinghast Reflector Echelle Spectrograph (TRES; Szentgyorgyi & Furész 2007) on the 1.5 m telescope at the Fred L. Whipple Observatory on Mt. Hopkins, AZ. The TRES spectra have a resolution of 44,000 and were extracted as described in Buchhave et al. (2010). We obtained 8 TRES spectra of HD 286123 in 2017 October. The average S/N per resolution element (SNRe) was 46, which was determined at the peak continuum of the Mgb region of the spectrum near 519 nm. HD 89345 was observed twice, once in 2017 November and again in 2017 Dec, with an average S/N of 54. The TRES spectra were not used to determine an orbital solution but were used to determine stellar parameters (see Section 3).

The RV data set for HD 286123 is comprised of 19 velocities obtained between 2018 October and 2019 February using the Automated Planet Finder (APF), a 2.4 m telescope located atop Mt. Hamilton at Lick Observatory. The telescope is paired with the Levy echelle spectrograph, and is capable of reaching $1\,\mathrm{m\,s^{-1}}$ precision on bright, quiet stars. The Levy spectrograph is operated at a resolution of $\sim$90,000 for RV observations and covers a wavelength range of 370–900 nm, though only the 500–620 nm iodine region is used in extracting Doppler velocities (Vogt et al. 2014). APF RVs were collected using the same iodine-based methodology described above.

The APF is a dedicated exoplanet facility, and employs a dynamic scheduler to operate without the aid of human observers (Burt et al. 2015). Due to the large expected RV semi-amplitude of the transiting planet ($K \sim 26\,\mathrm{m\,s^{-1}}$) and the desire to use the telescope as efficiently as possible, we set the desired RV precision in the dynamic scheduler to $4\,\mathrm{m\,s^{-1}}$. The exposure times necessary to achieve this precision were automatically calculated in real time to account for changing atmospheric conditions, and the resulting RV data set has a mean internal uncertainty of $3.9\,\mathrm{m\,s^{-1}}$. In our analysis, we chose to omit data taken on one night due to a low number of photons in the iodine region, caused by cloudy observing conditions.

APF RVs for HD 89345 were collected in exactly the same way between 2017 November and 2018 February except that we used fixed 30 minute exposure times giving S/N $\sim$ 80. We also utilized the iodine-free "template" observations collected on Keck during the RV extraction in order to avoid duplication of data. All RV measurements for the two systems are reported in Tables 2 and 3.

2.2.2. Keck/NIRC2 Adaptive Optics Imaging

We obtained NIR adaptive optics (AO) imaging of HD 89345 through clear skies with $\sim0\rlap{.}''8$ seeing on the night of 2017 December 29 using the 10 m Keck II telescope at the W. M. Keck Observatory. The star was observed behind the natural guide star AO system using the NIRC2 camera in narrow angle mode with the large hexagonal pupil. We observed using the narrowband Br-γ filter ($\lambda_c = 2.1686\,\mu$m; $\Delta\lambda = 0.0326\,\mu$m) with a 3-point dither pattern that avoids the noisier lower left quadrant of the NIRC2 detector. Each dither was offset from the previous position by $0\rlap{.}''5$ and the star was imaged at nine different locations across the detector. The integration time per dither was 1 s for a total time of 9 s. The narrow angle mode of NIRC2 provides a field of view of $10''$ and a plate scale of about $0\rlap{.}''01\,\mathrm{pixel^{-1}}$. We used the dithered images to remove sky

Table 2
Radial Velocities for HD 89345

$\mathrm{BJD_{TDB}}$	RV ($\mathrm{m\,s^{-1}}$)	σ_{RV} ($\mathrm{m\,s^{-1}}$)	Instrument
2458088.069276	9.1	2.5	APF
2458089.027427	14.0	2.4	APF
2458092.004495	−7.8	1.9	HIRES
2458093.080794	−4.4	4.8	APF
2458094.982520	−2.0	2.5	APF
2458099.986259	5.6	1.7	HIRES
2458107.007150	−9.6	2.4	APF
2458109.930945	−6.0	3.5	APF
2458113.049078	2.9	1.4	HIRES
2458114.005711	6.4	2.8	APF
2458114.048573	2.3	1.7	HIRES
2458115.846145	−0.5	3.6	APF
2458116.934534	−8.5	1.2	HIRES
2458118.934942	−8.0	1.6	HIRES
2458120.050818	−8.9	2.8	APF
2458125.024846	1.0	1.7	HIRES
2458161.055191	1.7	1.2	HIRES
2458181.912190	5.3	1.6	HIRES
2458194.946988	14.0	1.6	HIRES
2458199.783821	−14.7	1.8	HIRES
2458209.952119	−0.3	1.8	HIRES

Table 3
Radial Velocities for HD 286123

$\mathrm{BJD_{TDB}}$	RV ($\mathrm{m\,s^{-1}}$)	σ_{RV} ($\mathrm{m\,s^{-1}}$)	Instrument
2458054.788304514	−0.6	3.1	APF
2458055.777965865	8.7	3.1	APF
2458070.727222747	−28.0	3.6	APF
2458076.725029452	−2.1	4.7	APF
2458079.684549427	1.4	2.9	APF
2458085.797267544	−30.0	3.0	APF
2458089.686288970	2.6	2.8	APF
2458097.641321792	−14.0	4.2	APF
2458098.690303951	−7.8	3.2	APF
2458099.706504478	1.1	2.7	APF
2458100.616924353	29.3	8.7	APF
2458102.620537149	4.8	3.2	APF
2458114.740644800	−13.0	4.0	APF

background, then aligned, flat-fielded, dark subtracted, and combined the individual frames into a final combined image (see Figure 2 inset). The final images had an FWHM resolution of $\sim$60 mas, near the diffraction limit at $\sim$2.2 μm.

We also obtained NIR high-resolution AO imaging of HD 286123 at Palomar Observatory with the $200''$ Hale Telescope at Palomar Observatory on 2017 September 06 using the NIR AO system P3K and the infrared camera PHARO (Hayward et al. 2001). PHARO has a pixel scale of $0\rlap{.}''025$ per pixel with a full field of view of approximately $25''$. The data were obtained with a narrowband Br-γ filter ($\lambda_o = 2.166$; $\Delta\lambda = 0.02\,\mu$m). The AO data were obtained in a 5-point quincunx dither pattern with each dither position separated by $4''$. Each dither position is observed three times with each pattern offset from the previous pattern by $0\rlap{.}''5$ for a total of 15 frames. The integration time per frame was 9.9 s for a total on-source time of 148.5 s. We use the dithered images to remove sky background and dark current, and then align, flat-field, and stack the individual images. The PHARO AO data have a resolution of $0\rlap{.}''10$ (FWHM).
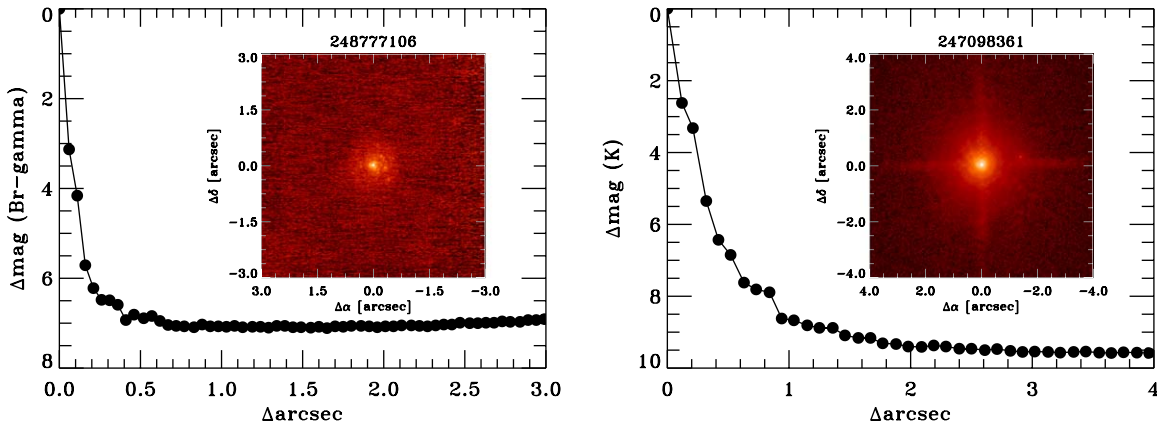
Figure 2. AO images (inset) and K_S-band contrast curves for HD 89345 (left) and HD 286123 (right). HD 89345 was imaged with Keck/NIRC2, and HD 286123 was imaged with Palomar/PHARO. The right image shows a faint companion at about $\sim 1\rlap{.}''4$ away from HD 286123, but this cannot be the source of the observed transit signals (see Section 2.2.2).

To determine the sensitivity of the final combined images, we injected simulated sources at positions that were integer multiples of the central source FWHM scaled to brightnesses where they could be detected at 5σ significance with standard aperture photometry. We compared the Δ-magnitudes of the injected 5σ sources as a function of their separation from the central star to generate contrast sensitivity curves (Figure 2). We were sensitive to close companions and background objects with ΔBr-$\gamma \approx 6$ at separations $\geqslant 200$ mas. No additional sources were detected down to this limit in the field of view of HD 89345, and the target appears single at the limiting resolution of the images.

A stellar companion was detected near HD 286123 in the Br-γ filter with PHARO. The companion separation was measured to be $\Delta\alpha = -1\rlap{.}''39 \pm 0\rlap{.}''01$ and $\Delta\delta = 0\rlap{.}''28 \pm 0\rlap{.}''03$. The companion has a measured differential brightness in comparison to the primary star of $\Delta_K = 6.75 \pm 0.05$ mag, which implies deblended stellar 2MASS K-band magnitudes of $K_S = 8.45 \pm 0.02$ mag and $K_S = 15.2 \pm 0.1$ mag for the primary and the companion respectively. Utilizing Kepler magnitude (K_p)-K_S relationships from Howell et al. (2012), we derive approximate deblended Kepler magnitudes of $K_p = 9.81 \pm 0.01$ mag for the primary and $K_p = 17.3 \pm 0.8$ mag for the companion. The resulting Kepler magnitude difference is $\Delta K_p = 7.5 \pm 0.8$ mag. The companion star therefore cannot be responsible for the transit signals, but is potentially a bound stellar companion. At a separation of $1\rlap{.}''4$, the projected separation of the companion is approximately 175 au. This translates to an orbital period of about ~ 2300 years (10^6 days), which is near the peak of the period distribution of binaries (Raghavan et al. 2010) and within the 80% likelihood of AO-detected companions being bound for these separations (Hirsch et al. 2017). With an infrared magnitude difference of $\Delta_K = 6.75$ mag and assuming the distance of HD 286123, the companion star has an infrared magnitude similar to that of an M7V dwarf (Pecaut & Mamajek 2013).

The AO imaging rules out the presence of any additional stars within $\sim 0\rlap{.}''5$ of HD 286123 (~ 30 au) and the presence of any brown dwarfs, or widely separated tertiary components down to $K_S = 16.4$ beyond $0\rlap{.}''5$ (~ 30–1000 au). All data and sensitivity curves are available on the ExoFOP-K2 site.[24]

We also searched for any faint sources within the $K2$ apertures used but beyond the field of view of the AO imaging
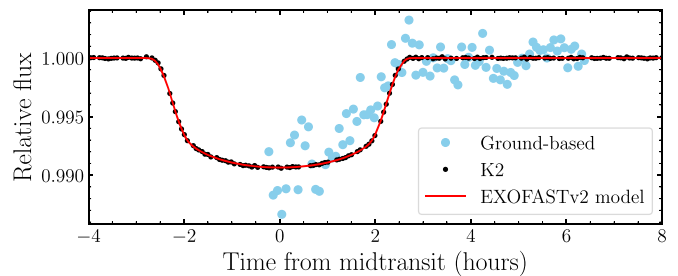
---

[24] https://exofop.ipac.caltech.edu

Figure 3. Detrended ground-based light curve of HD 286123 (blue) and $K2$ light curve (black) phase-folded to the same ephemeris and overplotted with the transit model (red) from our global fit in Section 4.1.

by examining archival images from imaging surveys including SDSS9, 2MASS, Pan-STARRS, and DECaLS/DR3, and catalogs including UCAC, GSC2.3, 2MASS, and SDSS12. Across all surveys and catalogs, we identified no sources brighter than 19 mag in the g'-band and 18 mag in the r'-band within $40''$ of either star. The optical flux contribution of any faint companion is below the precision of $K2$ and can be safely ignored in our transit fits.

2.2.3. Ground-based Photometry

We obtained additional ground-based photometric observations of HD 286123 on the night of 2017 September 29. One of us (G.M.) observed the second half of the transit from Suwałki, Poland, using a 78 mm ASI178MM-cooled camera with a $1/1\rlap{.}''8$ CMOS IMX178 sensor and Canon FD 300 mm $f/2.8$ lens. The images have pixel scales of $1\rlap{.}''65$/pixel. No filter was used, and each measurement consists of 100 binned 3 s exposures.

Dark and flat calibrations were applied to each frame. The aperture used was a circular aperture with a radius corresponding to $8\rlap{.}''7$. Two stable stars within the field of view were used as reference stars, and the flux of HD 286123 was divided by the sum of the reference stars' fluxes. We modeled the out-of-transit variations with a quadratic function, which was also divided out to obtain the detrended light curve. Figure 3 shows the resulting light curve overplotted with the $K2$ light curve, phase-folded to the same ephemeris. The data clearly show the transit egress and so confirm the ephemeris of this planet, but in the rest of our analysis we use only the $K2$ light curve.

Table 4
Median Values and 68% Confidence Intervals for the Physical and Orbital Parameters of the HD 89345 and HD 286123 Systems

Parameter	Units	HD 89345 Solution 1 (subgiant)	HD 89345 Solution 2 (main sequence)	HD 286123
Stellar Parameters				
M_*	Mass ($M_\odot$)	$1.157^{+0.040}_{-0.045}$	$1.324^{+0.044}_{-0.041}$	$1.039^{+0.071}_{-0.065}$
R_*	Radius ($R_\odot$)	$1.747^{+0.049}_{-0.050}$	1.733 ± 0.047	$1.233^{+0.026}_{-0.025}$
L_*	Luminosity ($L_\odot$)	$2.66^{+0.15}_{-0.16}$	2.71 ± 0.15	$1.646^{+0.080}_{-0.079}$
ρ_*	Density (cgs)	$0.305^{+0.027}_{-0.025}$	$0.359^{+0.029}_{-0.026}$	$0.782^{+0.077}_{-0.070}$
$\log g$	Surface gravity (cgs)	4.016 ± 0.026	$4.083^{+0.023}_{-0.022}$	4.273 ± 0.035
$T_{\rm eff}$	Effective Temperature (K)	5576^{+73}_{-76}	5622^{+70}_{-71}	5888^{+71}_{-77}
[Fe/H]	Metallicity	$0.421^{+0.046}_{-0.054}$	$0.436^{+0.040}_{-0.050}$	$0.051^{+0.058}_{-0.056}$
Age	Age (Gyr)	$7.53^{+1.3}_{-0.99}$	$4.18^{+0.64}_{-0.69}$	$7.1^{+3.1}_{-2.7}$
A_v	V-band extinction	$0.017^{+0.012}_{-0.011}$	0.017 ± 0.012	$0.017^{+0.012}_{-0.011}$
$\sigma_{\rm SED}$	SED photometry error scaling	$5.4^{+2.2}_{-1.3}$	$5.2^{+2.1}_{-1.3}$	$3.28^{+1.3}_{-0.82}$
d	Distance (pc)	$132.8^{+1.8}_{-1.7}$	132.7 ± 1.7	131.7 ± 1.7
π	Parallax (mas)	7.533 ± 0.098	$7.533^{+0.098}_{-0.097}$	$7.594^{+0.10}_{-0.098}$
Planet Parameters				
P	Period (days)	11.81430 ± 0.00020	$11.81430^{+0.00020}_{-0.00019}$	11.168459 ± 0.000017
R_P	Radius ($R_{\rm J}$)	$0.660^{+0.028}_{-0.030}$	$0.648^{+0.029}_{-0.030}$	$1.058^{+0.023}_{-0.022}$
T_C	Time of Transit (BJD$_{\rm TDB}$)	$2457913.8052^{+0.0011}_{-0.0010}$	$2457913.80504^{+0.0011}_{-0.00094}$	$2457858.856812^{+0.000042}_{-0.000046}$
a	Semimajor axis (au)	$0.1066^{+0.0012}_{-0.0014}$	0.1115 ± 0.0012	$0.0991^{+0.0022}_{-0.0021}$
i	Inclination (Degrees)	$87.21^{+0.43}_{-0.22}$	$87.56^{+0.59}_{-0.24}$	$89.61^{+0.26}_{-0.29}$
e	Eccentricity	$0.220^{+0.095}_{-0.13}$	$0.22^{+0.10}_{-0.12}$	$0.255^{+0.034}_{-0.036}$
ω_*	Argument of Periastron (Degrees)	-13^{+58}_{-27}	-16^{+56}_{-27}	$170.9^{+5.7}_{-340}$
$T_{\rm eq}$	Equilibrium temperature (K)	1089^{+15}_{-16}	1068^{+14}_{-15}	1001 ± 14
M_P	Mass ($M_{\rm J}$)	$0.110^{+0.017}_{-0.018}$	$0.121^{+0.018}_{-0.019}$	$0.387^{+0.044}_{-0.042}$
K	RV semi-amplitude (m s^{-1})	9.2 ± 1.5	9.2 ± 1.5	$35.4^{+4.6}_{-4.3}$
$\log K$	Log of RV semi-amplitude	$0.962^{+0.064}_{-0.080}$	$0.965^{+0.064}_{-0.078}$	$1.550^{+0.053}_{-0.056}$
R_P/R_*	Radius of planet in stellar radii	$0.0389^{+0.0011}_{-0.0012}$	0.0384 ± 0.0012	$0.08811^{+0.00031}_{-0.00017}$
a/R_*	Semimajor axis in stellar radii	$13.11^{+0.38}_{-0.36}$	$13.84^{+0.36}_{-0.34}$	$17.28^{+0.55}_{-0.53}$
δ	Transit depth (fraction)	$0.001509^{+0.000085}_{-0.000091}$	$0.001477^{+0.000094}_{-0.000090}$	$0.007764^{+0.000054}_{-0.000030}$
Depth	Flux decrement at mid transit	$0.001509^{+0.000085}_{-0.000091}$	$0.001477^{+0.000094}_{-0.000090}$	$0.007764^{+0.000054}_{-0.000030}$
τ	Ingress/egress transit duration (days)	$0.0149^{+0.0045}_{-0.0037}$	$0.0135^{+0.0046}_{-0.0034}$	$0.01717^{+0.00047}_{-0.00020}$
T_{14}	Total transit duration (days)	$0.2389^{+0.0037}_{-0.0033}$	$0.2378^{+0.0038}_{-0.0030}$	$0.20959^{+0.00033}_{-0.00028}$
$T_{\rm FWHM}$	FWHM transit duration (days)	0.2239 ± 0.0016	0.2241 ± 0.0016	$0.19233^{+0.00026}_{-0.00027}$
b	Transit Impact parameter	$0.645^{+0.089}_{-0.15}$	$0.60^{+0.11}_{-0.19}$	$0.108^{+0.080}_{-0.072}$
b_S	Eclipse impact parameter	$0.568^{+0.057}_{-0.079}$	$0.509^{+0.051}_{-0.077}$	$0.114^{+0.082}_{-0.076}$
τ_S	Ingress/egress eclipse duration (days)	$0.0129^{+0.0018}_{-0.0020}$	$0.0114^{+0.0013}_{-0.0016}$	$0.0182^{+0.0011}_{-0.0010}$
$T_{S,14}$	Total eclipse duration (days)	$0.232^{+0.030}_{-0.021}$	$0.226^{+0.039}_{-0.026}$	$0.221^{+0.013}_{-0.012}$
$T_{S,\rm FWHM}$	FWHM eclipse duration (days)	$0.219^{+0.029}_{-0.018}$	$0.215^{+0.038}_{-0.024}$	$0.202^{+0.012}_{-0.011}$
$\delta_{S,3.6\,\mu m}$	Blackbody eclipse depth at 3.6 μm (ppm)	$40.0^{+3.1}_{-3.3}$	36.0 ± 2.9	$136.9^{+7.6}_{-7.4}$
$\delta_{S,4.5\,\mu m}$	Blackbody eclipse depth at 4.5 μm (ppm)	$65.3^{+4.7}_{-5.1}$	$59.7^{+4.6}_{-4.5}$	$239^{+11}_{-10.}$
ρ_P	Density (cgs)	$0.471^{+0.094}_{-0.084}$	$0.547^{+0.11}_{-0.096}$	$0.405^{+0.046}_{-0.044}$
$\log g_P$	Surface gravity	$2.795^{+0.068}_{-0.079}$	$2.852^{+0.066}_{-0.076}$	$2.933^{+0.045}_{-0.048}$
$\langle F \rangle$	Incident Flux (10^9 erg s^{-1} cm^{-2})	$0.303^{+0.021}_{-0.022}$	$0.280^{+0.019}_{-0.020}$	0.214 ± 0.011
T_P	Time of Periastron (BJD$_{\rm TDB}$)	$2457911.30^{+1.5}_{-0.89}$	$2457911.23^{+1.4}_{-0.89}$	$2457860.59^{+0.24}_{-0.20}$
T_S	Time of eclipse (BJD$_{\rm TDB}$)	$2457909.29^{+0.65}_{-1.1}$	$2457909.33^{+0.63}_{-1.1}$	$2457862.67^{+0.25}_{-0.23}$
T_A	Time of Ascending Node (BJD$_{\rm TDB}$)	$2457911.42^{+0.36}_{-0.43}$	$2457911.40^{+0.35}_{-0.42}$	2457855.32 ± 0.17
T_D	Time of Descending Node (BJD$_{\rm TDB}$)	$2457917.54^{+1.0}_{-0.84}$	$2457917.62^{+1.1}_{-0.88}$	$2457860.70^{+0.15}_{-0.14}$
$e\cos\omega_*$		$0.185^{+0.087}_{-0.15}$	$0.189^{+0.084}_{-0.15}$	$-0.252^{+0.036}_{-0.033}$
$e\sin\omega_*$		$-0.03^{+0.12}_{-0.13}$	$-0.04^{+0.12}_{-0.14}$	0.026 ± 0.029
$M_P\sin i$	Minimum mass ($M_{\rm J}$)	$0.110^{+0.017}_{-0.018}$	$0.121^{+0.018}_{-0.019}$	$0.387^{+0.044}_{-0.042}$
M_P/M_*	Mass ratio	$0.000091^{+0.000014}_{-0.000015}$	$0.000087^{+0.000013}_{-0.000014}$	$0.000355^{+0.000047}_{-0.000044}$
d/R_*	Separation at mid transit	$13.1^{+1.4}_{-1.5}$	$13.9^{+1.5}_{-1.6}$	$15.8^{+1.1}_{-1.0}$
Wavelength Parameters	**Kepler**			
$u_{1,Kepler}$	linear limb-darkening coeff	0.437 ± 0.038	$0.432^{+0.037}_{-0.038}$	0.412 ± 0.011
$u_{2,Kepler}$	quadratic limb-darkening coeff	$0.206^{+0.046}_{-0.045}$	0.214 ± 0.046	0.211 ± 0.027

Table 4
(Continued)

Parameter	Units	HD 89345		HD 286123
		Solution 1 (subgiant)	Solution 2 (main sequence)	
Telescope Parameters	Kepler			
γ	APF instrumental offset (m s^{-1})	$0.2^{+1.8}_{-1.7}$	0.2 ± 1.7	-11.8 $\pm$ 2.2
γ	HIRES instrumental offset (m s^{-1})	$-3.0^{+1.7}_{-1.6}$	$-3.1^{+1.7}_{-1.6}$	...
σ_J	APF RV jitter	$4.2^{+2.9}_{-2.2}$	$4.1^{+2.9}_{-2.2}$	$3.7^{+1.6}_{-1.4}$
σ_J	HIRES RV jitter	$4.1^{+1.5}_{-1.1}$	$4.0^{+1.5}_{-1.1}$	...
σ_J^2	APF RV jitter variance	17^{+33}_{-14}	16^{+33}_{-13}	$13.8^{+15}_{-8.4}$
σ_J^2	HIRES RV jitter variance	$16.4^{+15}_{-7.5}$	$16.3^{+14}_{-7.4}$	...
Transit Parameters	Kepler			
σ^2	Added Variance	$0.00000000007^{+0.0000000050}_{-0.0000000045}$	$0.00000000006^{+0.0000000051}_{-0.0000000045}$	$0.00000000038^{+0.0000000015}_{-0.0000000013}$
F_0	Baseline flux	0.9999984 ± 0.0000050	0.9999983 ± 0.0000051	0.9999994 ± 0.0000027

3. Host Star Characterization

3.1. Spectral Analysis

We searched the iodine-free Keck/HIRES for spectroscopic blends using the algorithm of Kolbl et al. (2015), which is sensitive to secondary stars with >1% flux and ΔRV > 10 km s^{-1} relative to the primary star. No secondary lines were detected in either spectrum.

We calculated initial estimates of the spectroscopic parameters of the host stars from our iodine-free Keck/HIRES spectra using the SpecMatch procedure (Petigura 2015). SpecMatch searches a grid of synthetic model spectra (Coelho et al. 2005) to fit for the effective temperature ($T_{\rm eff}$), surface gravity (log g), metallicity ([Fe/H]), and projected equatorial rotation velocity of the star ($v \sin i$). The resulting values are $T_{\rm eff} = 5532 \pm 100$ K, log $g = 3.71 \pm 0.10$, [Fe/H] = $+0.44 \pm 0.06$, $v \sin i = 3 \pm 1$ km s^{-1} for HD 89345, and $T_{\rm eff} = 5909 \pm 100$ K, log $g = 4.25 \pm 0.10$, [Fe/H] = $+0.05 \pm 0.06$, $v \sin i = 3 \pm 1$ km s^{-1} for HD 286123. We adopt these values as starting points and/or priors for the `isoclassify` fits described in Section 3.2 and the global fit described in Section 4.1.

As a consistency check, we also estimated the spectroscopic parameters using our TRES spectra and the Stellar Parameter Classification tool (SPC; Buchhave et al. 2012, 2014). SPC works by cross-correlating observed spectra with a grid of synthetic model spectra generated from Kurucz (1992) model atmospheres. From these fits, we obtained weighted averages of $T_{\rm eff} = 5676 \pm 50$ K, log $g = 4.13 \pm 0.10$, [Fe/H] = $+0.50 \pm 0.08$, $v \sin i = 3.3 \pm 0.5$ km s^{-1} for HD 89345, and $T_{\rm eff} = 5877 \pm 53$ K, log $g = 4.27 \pm 0.10$, [Fe/H] = $+0.03 \pm 0.08$, $v \sin i = 3.9 \pm 0.5$ km s^{-1} for HD 286123. The values from SPC are in agreement with those from SpecMatch, except for the slightly higher log g value for HD 89345 from SPC. Given that HD 89345 is a slightly evolved star, spectroscopic log g estimates are expected to be less reliable. As shown by Torres et al. (2012), reliance on spectroscopically determined log g can lead to considerable biases in the inferred evolutionary state, mass, and radius of a star. Therefore, we avoid imposing any priors on log g for our global fit in Section 4.1.

3.2. Evolutionary Analysis

We then use the stellar parameters derived from HIRES spectra as well as broadband photometry and parallax as inputs for the grid-modeling method implemented in the stellar classification package `isoclassify` (Huber et al. 2017). `isoclassify` derives posterior distributions for stellar parameters ($T_{\rm eff}$, log g, [Fe/H], radius, mass, density, luminosity, and age) through direct integration of isochrones from the MIST database (Choi et al. 2016; Dotter 2016) and synthetic photometry. Both target stars have parallaxes from Gaia DR2, but are saturated in the Sloan z band. We therefore input for each star its 2MASS JHK and Tycho BV magnitudes, Gaia parallax, and $T_{\rm eff}$, log g, and [Fe/H] from SpecMatch. The V-band extinction A_V is left as a free parameter. From this fit, we obtained $R_\star = 1.720 \pm 0.051\,R_\odot$ and $M_\star = 1.147 \pm 0.034\,M_\odot$ for HD 89345 and $R_\star = 1.214 \pm 0.043\,R_\odot$ and $M_\star = 1.063 \pm 0.047\,M_\odot$ for HD 286123. These values are consistent with the final determined stellar parameters from our EXOFASTv2 global fit (See Table 4).

3.3. UVW Space Motions, Galactic Coordinates, and Evolutionary States of the Host Stars

To calculate the absolute RVs of the two host stars, we used the TRES observation with the highest S/N for each and corrected for the gravitational redshift by adding -0.61 km s^{-1}. This gives us an absolute velocity of 2.4 km s^{-1} for HD 89345 and 22.4 km s^{-1} for HD 286123. We quote an uncertainty of 0.1 km s^{-1}, which is an estimate of the residual systematics in the IAU RV standard star system.

3.3.1. HD 89345

HD 89345 is located at equatorial coordinates $\alpha = 10^{\rm h}18^{\rm m}41^{\rm s}.06$, and $\delta = +10°07'44''.5$ (J2000), which corresponds to Galactic coordinates of $\ell = 230°.8$ and $b = 50°.2$. Given the Gaia distance of ~127 pc, HD 89345 lies roughly 100 pc above the Galactic plane. Using the Gaia DR2 proper motion of $(\mu_\alpha, \mu_\delta) = (5.348 \pm 0.079, -42.449 \pm 0.071)$ mas yr^{-1}, the Gaia parallax, and the absolute RV as determined from the TRES spectroscopy of 2.4 ± 0.1 km s^{-1}, we find that HD 89345 has a three-dimensional Galactic space motion of $(U, V, W) = (21.5 \pm 0.1, -9.8 \pm 0.1, 1.5 \pm 0.1)$ km s^{-1}, where positive U is in the direction of the Galactic center, and we have adopted the Coşkunoğlu et al. (2011) determination of the solar motion with respect to the local standard of rest. These values yield a 99.4% probability that HD 89345 is a thin disk star, according to the classification scheme of Bensby et al. (2003).

Note that stars of the mass of HD 89345 ($M_\star \sim 1.2\,M_\odot$) that are close to the zero age main sequence typically have spectral

types of roughly F5V–F8V (Pecaut & Mamajek 2013), but in fact HD 89345 has a $T_{\rm eff}$ and colors that are more consistent with a much later spectral type of G5V–G6V (Pecaut & Mamajek 2013). Furthermore, it has a radius of $R \sim 1.74\,R_\odot$; much larger than one would expect of its mass if it were on the zero age main sequence. All of this implies that HD 89345 has exhausted or nearly exhausted its core hydrogen, and is currently in or close to the relatively short subgiant phase of its evolution, as it moves toward the giant branch. The location of HD 89345 above the disk (Bovy 2017) and Galactic velocities are all consistent with this scenario.

This conclusion is corroborated by the properties of the star inferred from the global fit to the transit, RV, spectral energy distribution (SED), and parallax data described in Section 4.1. A joint fit to these data measure, nearly directly and empirically, the stellar radius, density, surface gravity, and luminosity. As we note in Section 4.1, the global fit in fact yields two solutions, one on the main sequence and one on the subgiant branch. Together with the $T_{\rm eff}$ and [Fe/H], we can locate both of these solutions on a "theoretical" Hertzsprung–Russell diagram (see Figure 7). When comparing these values to MIST evolutionary tracks (Choi et al. 2016; Dotter 2016), we infer that HD 89345 has an age of either ~ 4.2 Gyr or 7.5 Gyr and is indeed either near or just past the end of its main-sequence lifetime.

3.3.2. HD 286123

HD 286123 is located at equatorial coordinates $\alpha = 4^{\rm h}55^{\rm m}03\!\overset{\rm s}{.}9$, and $\delta = +18°39'16\!\overset{''}{.}33$ (J2000), which correspond to the Galactic coordinates of $\ell = 182\!\overset{\circ}{.}1$ and $b = -15\!\overset{\circ}{.}3$. Given the Gaia distance of ~ 126 pc, HD 89345 lies roughly 34 pc below the Galactic plane. Using the Gaia DR2 proper motion of $(\mu_\alpha, \mu_\delta) = (62.064 \pm 0.077, -48.245 \pm 0.051)$ mas yr^{-1}, the Gaia parallax, and the absolute RV as determined from the TRES spectroscopy of 22.4 ± 0.1 km s^{-1}, we find that HD 286123 has a three-dimensional Galactic space motion of $(U, V, W) = (-14.9 \pm 0.1, -34.5 \pm 0.3, 13.5 \pm 0.1)$ km s^{-1}, where again positive U is in the direction of the Galactic center, and we have adopted the Coşkunoğlu et al. (2011) determination of the solar motion with respect to the local standard of rest. These values yield a 98.3% probability that HD 286123 is a thin disk star, according to the classification scheme of Bensby et al. (2003).

Note that stars of the mass of HD 286123 typically have spectral types of roughly G1V (Pecaut & Mamajek 2013), and in fact HD 286123 has a $T_{\rm eff}$ and colors that are roughly consistent with this spectral type (Pecaut & Mamajek 2013). The radius and luminosity of HD 286123 are $R_* \sim 1.23\,R_\odot$ and $L_* \sim 1.65\,L_\odot$; again, these are roughly consistent, although slightly larger, than would be expected for a zero-age main-sequence star of its mass and spectral type (Pecaut & Mamajek 2013). The Galactic velocities of HD 286123 are somewhat larger than typical thin disk stars. Together, these pieces of information suggest that HD 286123 is likely a roughly solar-mass star, with an age that is somewhat larger than the average age of the Galactic thin disk, that is roughly 70% of the way through its main-sequence lifetime. Indeed, when combined with the estimate of its metallicity, we can roughly characterize HD 286123 as a slightly older, slightly more massive analog of the Sun.

As with HD 89345, this conclusion is corroborated by the properties of HD 286123 inferred from the global fit to the

transit, RV, SED, and parallax data described in Section 4.1. When comparing the log g and $T_{\rm eff}$ from the global fit to MIST evolutionary tracks (Choi et al. 2016; Dotter 2016), we infer that HD 286123 has an age of ~ 7.1 Gyr and is indeed just over halfway through its main-sequence lifetime.

4. Planet Characterization

4.1. EXOFASTv2 Global Fit

To determine the system parameters for both HD 89345 and HD 286123, we perform a simultaneous fit using exoplanet global fitting suite EXOFASTv2 (Eastman 2017). EXO-FASTv2 is based largely on the original EXOFAST (Eastman et al. 2013) but is now more flexible and can, among many other features, simultaneously fit multiple RV instruments and the SED along with the transit data. Specifically, for each system we fit the flattened *K2* light curve, accounting for the long cadence smearing; the SED; and the RV data. To constrain the stellar parameters, we used the MESA Isochrones & Stellar Tracks (MIST, Choi et al. 2016; Dotter 2016), the broadband photometry, and the parallax from Gaia summarized in Table 1. In addition, we set priors on $T_{\rm eff}$ and [Fe/H] from the Keck/HIRES spectra described in Section 3.1 and enforced upper limits on the *V*-band extinction from the Schlegel et al. (1998) dust maps of 0.035 for HD 89345 and 0.4765 for HD 286123. We used the online EXOFAST tool[25] to refine our starting values prior to the EXOFASTv2 fit.

We note that the fit yielded bimodal posterior distributions for the age and mass of HD 89345, with the age distribution showing peaks at 7.53 and 4.18 Gyr, and the mass peaking at $1.157\,M_\odot$ and $1.324\,M_\odot$. The two peaks correspond to two solutions with the star being a subgiant and a main-sequence dwarf respectively. This degeneracy is also present when we repeat our global fits using the integrated Yale–Yonsei stellar tracks (Yi et al. 2001) instead of MIST. We also attempted an empirical fit using only the transits, RVs, SED, broadband photometry, and Gaia parallax but no isochrones, and the resulting mass distribution, with error bars as large as 80%, does not offer any useful insight. This degeneracy may be broken with better constraints on the eccentricity of the planet or asteroseismic analyses,[26] but in this paper, we report both solutions agnostically. Even so, the resulting planet masses from these two solutions are consistent to within 1σ because the error on planet mass is dominated by the uncertainty on the RV semi-amplitude.

See Figure 1 for the final transit fits, Figures 4 and 5 for the final RV fits, Figure 6 for the final SED fit from our EXOFASTv2 global fit, and Figure 7 for the best-fit evolutionary tracks. The median values of the posterior distributions of the system parameters are shown in Table 4.

4.2. RV Analysis with RadVel

For comparison with EXOFASTv2, we also analyze the RV time series using another widely used, publicly available RV fitting package RadVel[27] (Fulton et al. 2017). We impose a Gaussian prior on the orbital period and times of conjunction of HD 89345 and HD 286123 with means and standard deviations

---

[25] http://astroutils.astronomy.ohio-state.edu/exofast/exofast.shtml
[26] In an independent discovery paper, Van Eylen et al. (2018) found a stellar mass consistent with the lower of the two masses through asteroseismology.
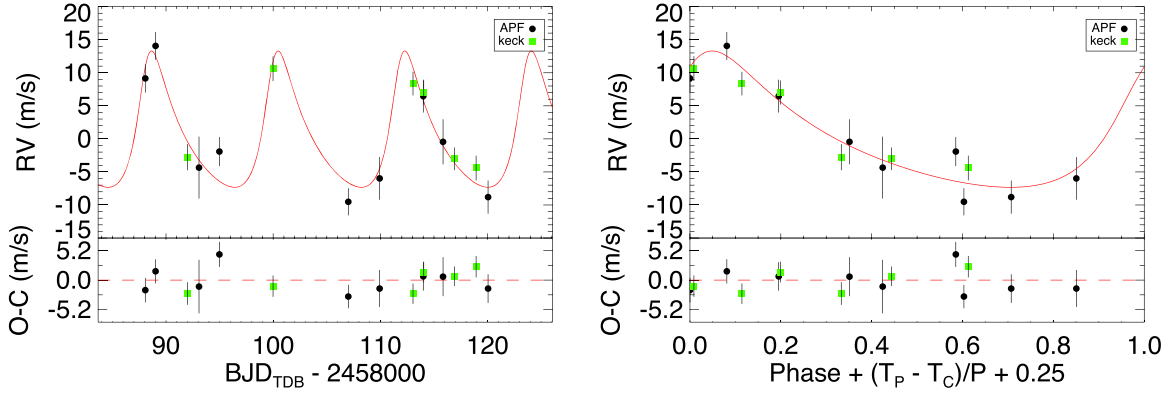[27] http://radvel.readthedocs.io/en/master/index.html

Figure 4. Left: the RV time series of HD 89345. In each panel, the green squares are the HIRES data and black circles are the APF data. The maximum-likelihood eccentric Keplerian orbital model is plotted in red. The instrumental offset has been subtracted from each data set and the model. The uncertainties plotted include the RV jitter terms listed in Table 4 added in quadrature with the measurement uncertainties for all RVs. Below are the residuals to the maximum-likelihood eccentric orbit model. Right: same as the left panel, but phase-folded to the best-fit ephemeris. The X-axis is defined such that the primary transit occurs at 0.25, where T_P is the time of periastron, T_C is the time of transit, and P is the period.
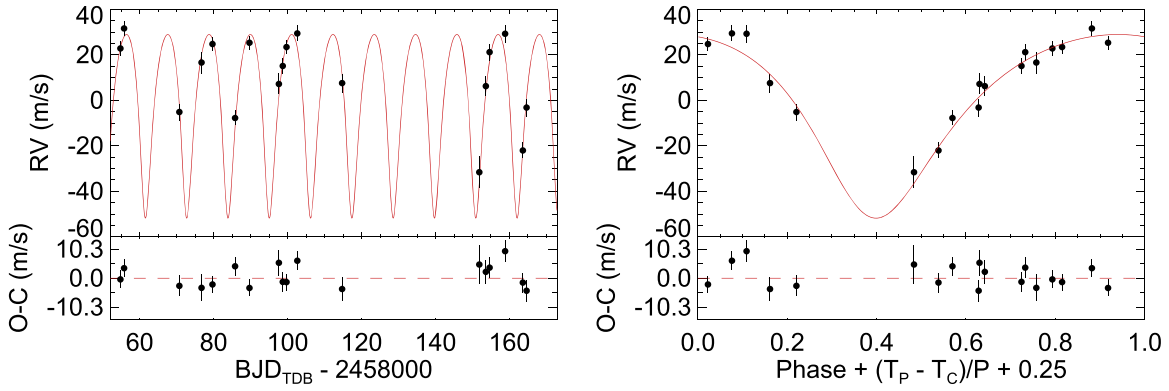
Figure 5. Same as Figure 4, but for HD 286123.
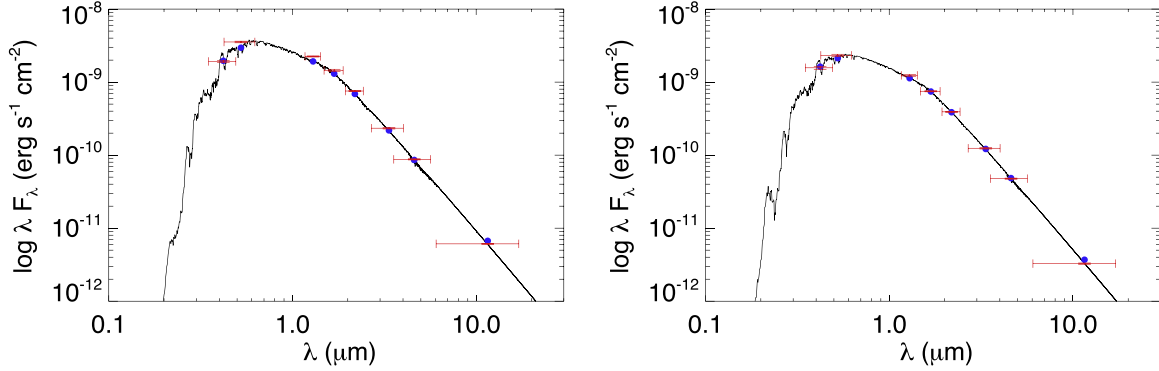
Figure 6. SED fits to HD 89345 (left) and HD 286123 (right) from EXOFASTv2. The red points show observed values, with the vertical error bars representing 1σ measurement uncertainties and horizontal error bars representing the widths of the bandpasses. The blue points are the model fluxes in the observed bandpasses. The solid lines show the model fits.

derived from transit photometry and given in Table 4. We initially included a constant radial acceleration term, dv/dt, but the result is consistent with zero for both systems. Therefore, we fix dv/dt to zero. The remaining free parameters are the velocity semiamplitudes, the zero-point offsets for each instrument, and the jitter terms for each instrument. The jitter terms are defined in Equation (2) of Fulton et al. (2015) and serve to capture the stellar jitter and instrument systematics such that the reduced χ^2 of the best-fit model is close to 1. To calculate $M_P \sin i$, we adopt the median stellar masses in Table 4 and their quoted error bars.

The fitting procedure is identical to that described in Sinukoff et al. (2016). The best-fit Keplerian orbital solutions are in agreement with those from EXOFASTv2 at the 1σ level.

5. Discussion

5.1. Potential for Atmospheric Characterization

Sub-Jovian gas giants are particularly interesting targets for atmospheric studies because a wide range of atmospheric compositions are possible. Yet the atmospheres of such planets, especially those more massive than Neptune but less massive

(a)

(b)

(c)
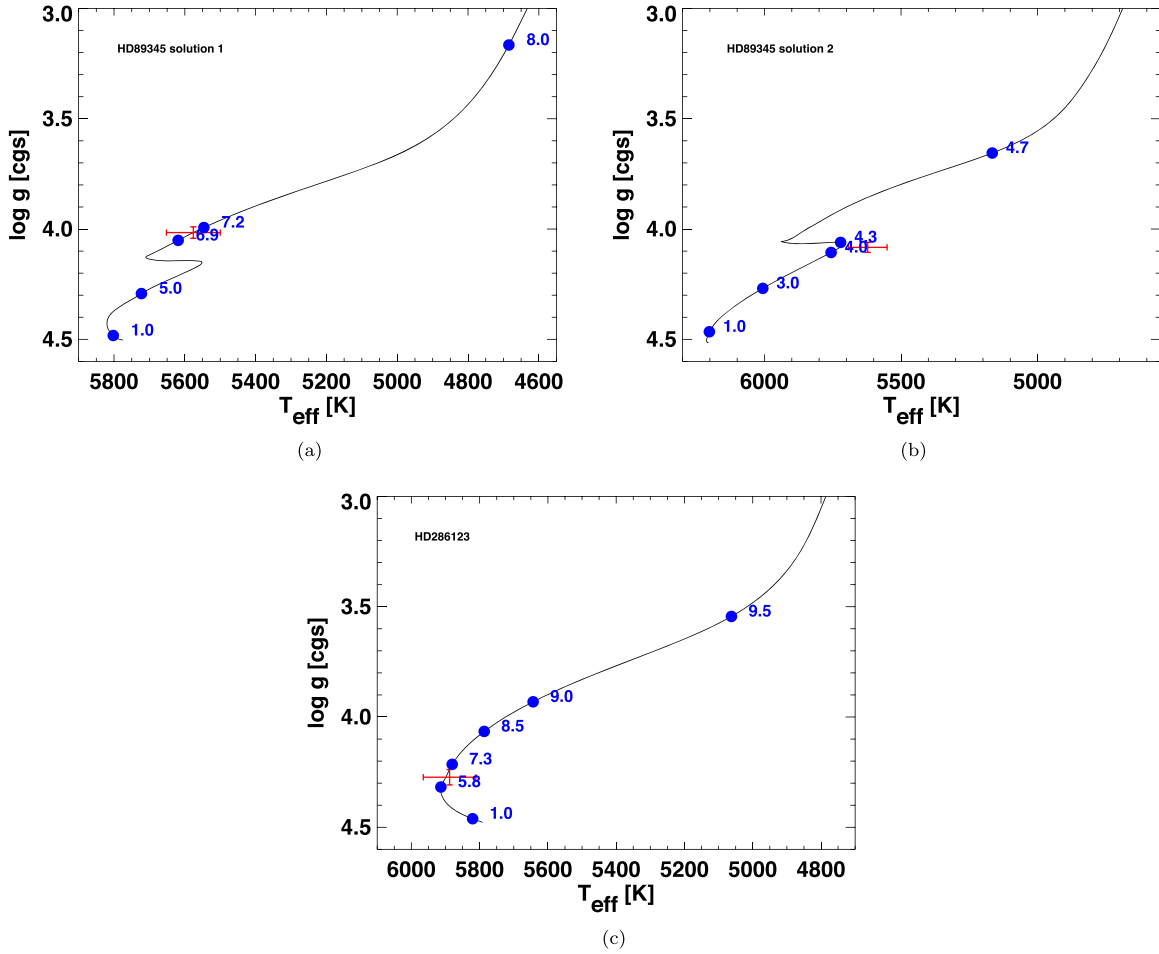
Figure 7. Locations of HD 89345 solution 1 (a), HD 89345 solution 2 (b) and HD 286123 (c) in the Kiel diagram. The median T_{eff} and log g from the global model fit are shown as red points, while the black lines show MIST evolutionary tracks for stars with best-fit values of $M_\star$ and [Fe/H]; the locations on the best-fit model corresponding to several values of stellar age are shown as blue points, with ages quoted in gigayears. The red points do not fall exactly on the evolutionary tracks at the median ages quoted in Table 4, because the median values in Table 4 are drawn from individual posterior distributions and are not always exactly self-consistent.

than Saturn, have not been thoroughly studied, both because the host stars of most such systems are too faint for atmospheric characterization, and because the mass regime of sub-Saturns is relatively unpopulated. The two systems presented in this paper are therefore important additions to the small sample of sub-Jovian gas giants amenable to atmospheric characterization.

With their bright host stars and low planet densities, both systems are promising targets for transit transmission spectroscopy. Such observations could provide insight into the planets' bulk composition and formation histories by measuring the elemental composition of their atmospheres, and overall metal enrichment. We calculated the expected S/N per transit compared to the expected scale height of each planet's atmosphere, and compared the results with other known transiting planets with $0.01\,M_J < M_p < 0.5\,M_J$. Specifically, we calculated the S/N as

$$\mathrm{S/N} \propto \frac{R_p H \sqrt{F t_{14}}}{R_\star^2}$$ (1)

$$H = \frac{k_b T_{eq}}{\mu g},$$ (2)

where R_p is the planet's radius, $R_\star$ is the star's radius, H is the planet atmosphere's scale height, k_b is Boltzmann's constant,

T_{eq} is the planet's equilibrium temperature, μ is the atmosphere's mean molecular weight, g is the planet's surface gravity, t_{14} is the transit duration, and F is the flux from the star. To simplify the comparison, we assumed the planets' atmospheres were dominated by molecular hydrogen and $\mu = 2$ for all cases. We also calculated F from the host stars' H-band magnitudes to test suitability for observations with the *Hubble Space Telescope*'s Wide Field Camera 3 instrument. Figure 8 shows the expected S/N for transmission spectroscopy (normalized such that the predicted S/N for WASP-107b is unity) against planet masses for HD 89345b, HD 286123b, and 30 known planets with the highest estimated S/N. For reference, Kreidberg et al. (2017) detected water features at 6.5σ confidence with a single *HST*/WFC3 transit observation of WASP-107b, the benchmark for comparison. HD 286123b appears to be one of the coolest Saturn-sized planets that are amenable to transmission spectroscopy. Notably, many known planets with the highest expected S/N, including GJ 1214b (Kreidberg et al. 2014), GJ 3470b (Ehrenreich et al. 2014), and GJ 436b (Knutson et al. 2014), were found to show essentially featureless transmission spectra, indicating the existence of hazes, clouds, or atmospheres with high molecular weight. So the estimated S/N does not necessarily mean that we will detect
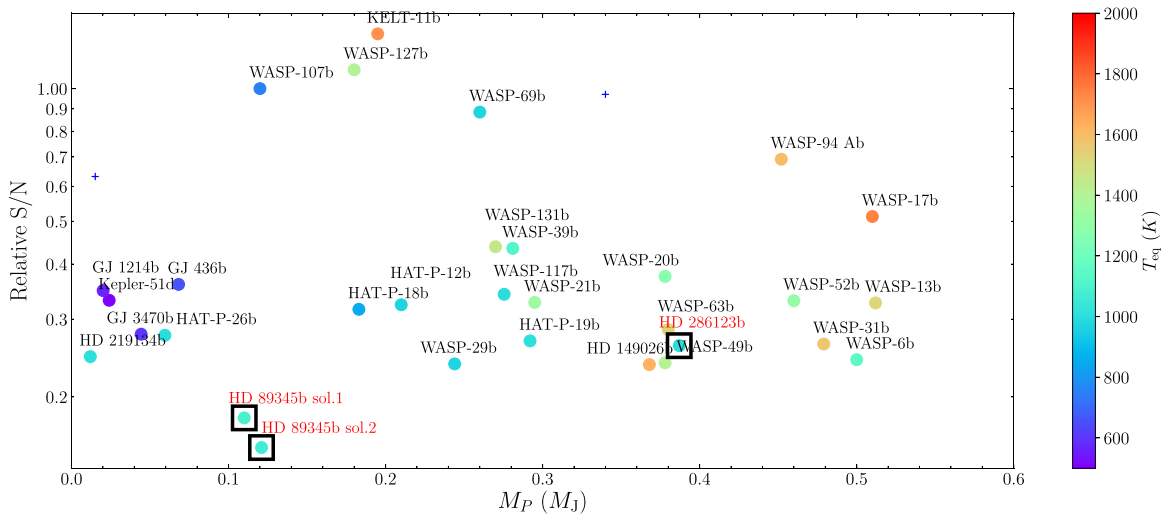
Figure 8. Estimated S/N per transit for transmission spectroscopy, relative to that of WASP-107b, as a function of planetary mass for planets with $0.01\,M_J < M_p < 0.5\,M_J$. Both solutions are shown for HD 89345b. Small plus symbols denote planets with uncertain mass and/or radius measurements (error >20%). Data retrieved from the NASA Exoplanet Archive on 2018 May 21.

spectral features in the atmospheres of HD 89345b and HD 286123b. Nevertheless, not all such planets have featureless spectra (Crossfield & Kreidberg 2017). Past works have found that a planet's likelihood of being cloudy/hazy is correlated with its equilibrium temperature: at temperatures below roughly 1000 K, methane is abundant and can easily photolyze to produce hydrocarbon hazes (e.g., Fortney et al. 2013; Morley et al. 2013). These predictions are borne out in observations of transmission spectra showing that hotter planets tend to have larger spectral features (e.g., Stevenson 2016; Crossfield & Kreidberg 2017; Fu et al. 2017). At $T_{eq} \approx 1000$ K, HD 89345b and HD 286123b are less likely to be hazy and there are fewer condensible cloud species. It is therefore scientifically compelling to pursue transmission spectroscopy for these planets, both to increase the small sample of Neptune- to Saturn-sized planets with well-characterized atmospheres and to inform the choice of which *TESS* planets to observe to efficiently study the atmospheric composition of sub-Jovian planets.

In addition to transit spectroscopy, HD 286123b is also a good candidate for secondary eclipse detection. Table 4 shows the blackbody eclipse depths at 3.6 and 4.5 μm, derived using the planet's equilibrium temperature assuming perfect redistribution and zero albedo, to test the feasibility of secondary eclipse observations with *Spitzer*. HD 286123b probes a different period, mass, and temperature range from most other planets with secondary eclipse detections, and is one of the few targets that are good candidates for both transmission spectroscopy and secondary eclipse observations.

5.2. The Evolutionary History of Close-in Giant Planets

Both planets fall in the same period range as warm Jupiters, giant planets with incident irradiation levels near or below $2 \times 10^8\,\mathrm{erg\,s^{-1}\,cm^{-2}}$, corresponding to orbital periods longer than 10 days around Sun-like stars (Shporer et al. 2017). Like hot Jupiters, they may have formed in situ, or migrated inward through high eccentricity migration or disk migration. But at wider orbital separations than hot Jupiters, the orbits of warm Jupiters are less likely to be perturbed by tides raised on the star, and their eccentricity and stellar obliquity distributions

may serve as the primordial (after emplacement) distributions for hot Jupiters. Previous works have found that the eccentricity distribution of warm Jupiters contains a low eccentricity component and a component with an approximately uniform distribution (Petrovich & Tremaine 2016). The former component cannot be easily explained by the high eccentricity tidal migration hypothesis, and the latter is a challenge for in situ formation or disk migration. This suggests that perhaps there is more than one migration mechanism at work.

Figure 9 shows HD 89345b and HD 286123b in a period-eccentricity diagram along with other known planets. HD 286123b has a moderately high eccentricity compared to planets at similar periods. The eccentricity of HD 89345b is only weakly constrained and driven away from zero largely by one data point. Given that, and the Lucy–Sweeney bias that tends to overestimate eccentricity due to the boundary at $e = 0$ (Lucy & Sweeney 1971), we cannot consider the eccentricity of HD 89345b to be significant without additional RV measurements. If these planets arrived at their present locations via high eccentricity migration, they must each be accompanied by a strong enough perturber to overcome precession caused by general relativity (Dong et al. 2014). Moreover, Dong et al. (2014) predicted that for warm Jupiters with orbital distances of 0.1–0.5 au, the perturbers must have separations of ~1.5–10 au (period 2–30 years). Although we detected no significant linear trend in the RVs of HD 89345 or HD 286123, long-term RV monitoring may be able to reveal the existence of any distant companions.

Both planets are also favorable targets for stellar obliquity measurements. Among hot Jupiter systems, spin–orbit misalignment is more commonly seen among hot stars ($T_{eff} \geqslant 6100$ K; Schlaufman 2010; Winn et al. 2010; Albrecht et al. 2012), and among the cooler stars, those hosting misaligned hot Jupiters are all in the zone $a_{min}/R_\star \geqslant 8$ (Dai & Winn 2017). Hot Jupiters also tend to be more misaligned at longer orbital periods (Li & Winn 2016). These observations have been construed as evidence for tidal realignment at work, but tidal realignment suffers from problems pointed out by Mazeh et al. (2015), who found that the hot/cool obliquity distinction persists even in cases where tidal interactions should
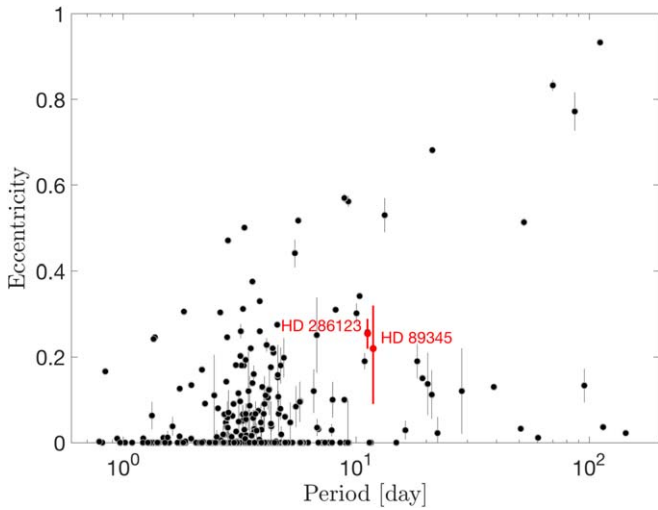
Figure 9. Orbital eccentricity vs. the log of the orbital period for transiting planets. The two new planets described in this paper are labeled and marked in red. Data retrieved from the NASA Exoplanet Archive on 2018 April 20.

be negligible. The interpretation of warm Jupiters' stellar obliquities remains an outstanding problem. Resolving this problem requires a larger observational sample size, yet the set of warm Jupiters (and smaller planets) currently available for obliquity studies is very small. Both planets in this paper have $a/R_\star$ values beyond the threshold for alignment found by Dai & Winn (2017), and the tidal effects on them are expected to be relatively weak. Measuring their stellar obliquities can potentially offer insight into their migration history and tidal realignment theories. One possible method is to measure the Rossiter–McLaughlin (RM) effect, whose maximum semi-amplitude is approximately

$$\Delta V_{\rm RM} \approx \left(\frac{R_P}{R_\star}\right)^2 \sqrt{1 - b^2}\,(v\sin i), \qquad (3)$$

where b is the impact parameter and $v\sin i$ is the projected equatorial rotation velocity of the star. Substituting values in Tables 1 and 4, we obtain $V_{\rm RM} \approx 4\,{\rm m\,s^{-1}}$ for HD 89345b and $V_{\rm RM} \approx 23\,{\rm m\,s^{-1}}$ for HD 286123b. Both should be detectable by modern spectrographs.

5.3. Constraining Planet Inflation Models

Many of the proposed mechanisms for explaining the inflated radii of giant planets are related to the irradiation the planet receives from its host star (cf. Burrows et al. 2007; Fortney et al. 2007). The relation to irradiation seems to be empirically confirmed. For example, radius enhancement is common if the planet receives at least $\sim 2 \times 10^8\,{\rm erg\,s^{-1}\,cm^{-2}}$, and mostly absent below that threshold (Demory & Seager 2011; Miller & Fortney 2011), and Hartman et al. (2016) argued that planets appear to reinflate when their stars increase in luminosity as they leave the main sequence.

HD 89345b and HD 286123b are gas giants on roughly 11 day period orbits around moderately evolved stars. At ages of roughly 4–7 Gyr, the host stars are near the end of or already leaving the main sequence. The time-averaged incident flux on the planets are given in Table 4 as $(3.03 \pm 0.22) \times 10^8\,{\rm erg\,s^{-1}\,cm^{-2}}$ (solution 1) or $(2.80 \pm 0.20) \times 10^8\,{\rm erg\,s^{-1}\,cm^{-2}}$ (solution 2) for HD 89345b and $(2.14 \pm 0.11) \times 10^8\,{\rm erg\,s^{-1}\,cm^{-2}}$ for HD 286123b, all just above the observed radius inflation threshold
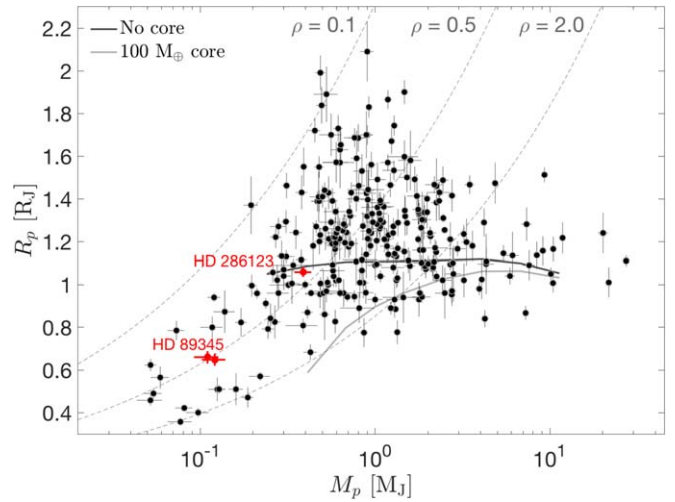
Figure 10. Radius–mass diagram (X-axis in log scale) of transiting planets with measured masses and radii, for planets with $R_p > 0.3\,R_{\rm J}$. The two new planets described in this paper are labeled and marked in red. For HD 89345, both solutions are marked in the plot. The thick solid and dashed lines show radius–mass models from Fortney et al. (2007) for gas giants with no solid core (thick solid black line) and a large core of $100\,M_\oplus$ (thick solid gray line). Also plotted are three equal density lines (dashed thin gray lines) with mean densities of $\langle\rho\rangle = 0.1,\ 0.5,$ and $2.0\,{\rm g\,cm^{-3}}$. Data retrieved from the NASA Exoplanet Archive on 2018 April 20.
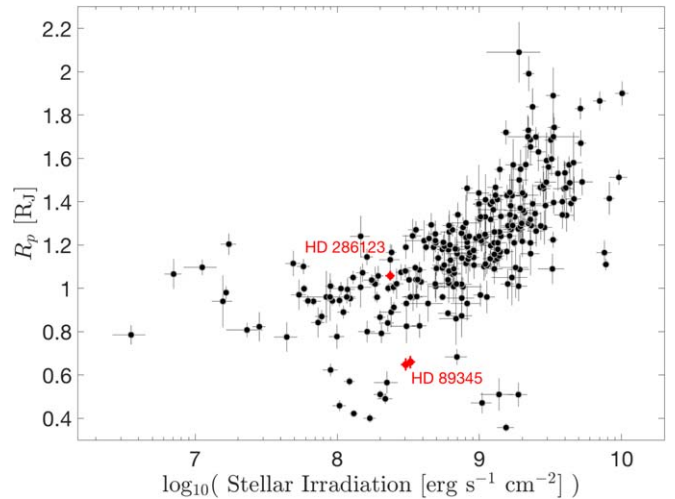

Figure 11. Planet radius vs. stellar irradiation at the planets' orbits for transiting planets with measured mass and radius, for planets with $R_p > 0.3\,R_{\rm J}$. The two new planets described in this paper are labeled and marked in red. For HD 89345, both solutions are marked in the plot. Data were retrieved from the NASA Exoplanet Archive on 2018 April 20.

found by Miller & Fortney (2011) and Demory & Seager (2011). Yet, when shown in a mass–radius diagram (Figure 10) alongside other planets with measured masses and radii, neither appears unusually large for its mass. The same conclusion can be drawn from Figure 11, where the radii of the two planets are compared with those of other planets at similar irradiation levels. Thus, despite being slightly above the critical insolation required for radius inflation, neither planet is significantly inflated.

To further examine the irradiation history of these two planets, we estimate the change in stellar irradiation over time using MIST evolutionary tracks (Choi et al. 2016; Dotter 2016) interpolated to stellar masses and metallicities derived in Section 4.1. Figure 12 shows the irradiation history of both planets as their host stars
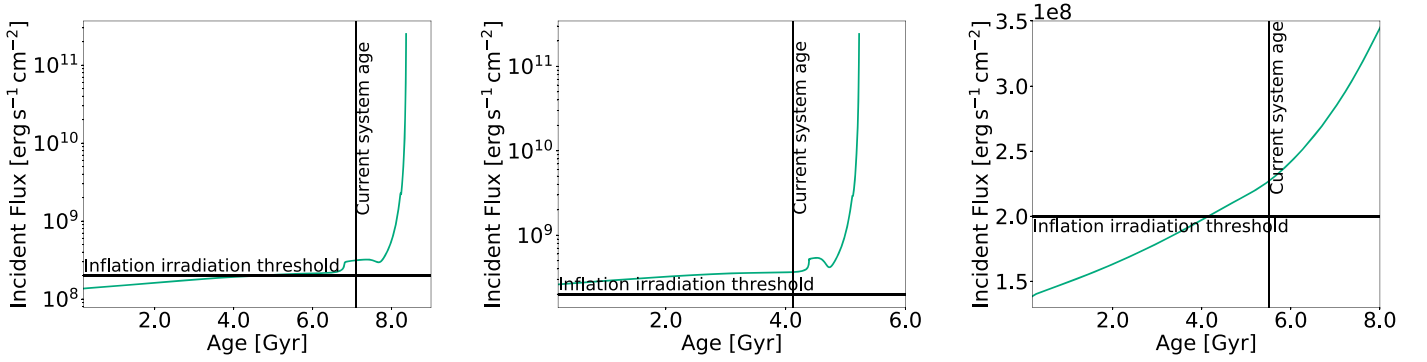
Figure 12. Models of the orbital evolution of HD 89345b solution 1 (left), HD 89345b solution 2 (middle), and HD 286123b (right) for tidal quality factors $Q'_\star \sim 10^5$ and $Q'_{\rm planet} \sim 10^6$. The horizontal line represents the threshold value of 2×10^8 erg s^{-1} cm^{-2} for radius inflation from Miller & Fortney (2011) and Demory & Seager (2011). The vertical lines show the current ages of the systems.

evolve. We conclude that for both planets, the orbit-averaged incident flux has been within a factor of two of the empirical critical value of $\sim 2 \times 10^8$ erg s^{-1} cm^{-2} at least as far back as the zero-age main-sequence phase of the host stars.

The above calculation ignores possible evolution in the orbits of the planets. This is justified by the absence of other bodies in the systems, since the only other mechanism for orbital evolution is tidal decay after the disk disappears, and for both systems the timescales of this process are rather long, even assuming efficient dissipation (tidal quality factors of $Q'_\star \sim 10^5$ and $Q'_{\rm planet} \sim 10^6$) and taking the present day planetary and stellar radii, which must have been smaller in the past. In particular, using Equations (1) and (2) from Jackson et al. (2009), the timescales for the evolution of the semimajor axis and the orbital eccentricity are approximately

$$\left(\frac{1}{a}\frac{da}{dt}\right)^{-1} \approx 210 \text{ Gyr (sol.1) or } 290 \text{ Gyr (sol.2)} \tag{4}$$

$$\left(\frac{1}{e}\frac{de}{dt}\right)^{-1} \approx 40 \text{ Gyr (sol.1) or } 50 \text{ Gyr (sol.2)} \tag{5}$$

for HD 89345b, and

$$\left(\frac{1}{a}\frac{da}{dt}\right)^{-1} \approx 85 \text{ Gyr} \tag{6}$$

$$\left(\frac{1}{e}\frac{de}{dt}\right)^{-1} \approx 20 \text{ Gyr} \tag{7}$$

for HD 286123b. Using $Q'_{\rm planet} \sim 10^5$ for HD 286123b results in an eccentricity decay timescale of just 3 Gyr, which conflicts with the observed nonzero eccentricity of the system.

The results of our calculation therefore apply to any dissipation less efficient that $Q'_\star \sim 10^5$ and $Q'_{\rm planet} \sim 10^6$. In this regime, both planets have been very close to the critical irradiation threshold throughout their lifetimes. Lopez & Fortney (2016) found that if the inflation mechanism operates by depositing some fraction of a planet's incident irradiation into its deep interior (class I), then a Saturn-mass planet on a 20 day orbit around a 1.5 $M_\odot$ star can rapidly inflate to more than 2 Jupiter radii as the host star leaves the main sequence. In contrast, a class II inflation mechanism that operates by delayed cooling should not cause a planet to inflate as its host evolves off the main sequence. We stress that the critical irradiation threshold is not known to better than a factor of two. That the two planets presented here are not inflated shows that if class I

mechanisms are indeed responsible for planet inflation, then these planets have not yet reached high enough irradiation levels or have not had time to inflate in response to increasing irradiation. Regardless, they probe the regime where inflation begins to be noticeable, and provide two new additions to the currently very small sample of warm gas giants to test the two theories. Moreover, most existing gas giant inflation studies have focused on Jupiter-mass objects, but these new detections are lower mass and could potentially provide interesting new insight into the physical processes governing inflation.

5.4. HD 89345b and the Transition between Ice Giants and Gas Giants

HD 89345b has a radius 0.8 times that of Saturn and a mass ~ 0.1 times that of Jupiter. It may therefore be a rare example of a sub-Saturn ($4\,R_\oplus < R_p < 8\,R_\oplus$, and $0.02\,M_{\rm J} \lesssim M_p \lesssim 0.2\,M_{\rm J}$, using the definition of Petigura et al. 2016). Apart from HD 89345b, there are only ~ 20 known sub-Saturns with masses determined to within 50% accuracy. In the core accretion scenario, rapid accretion of a gaseous envelope is expected to start in this mass regime (e.g., Mordasini et al. 2015). Sub-Saturns are therefore an important mass regime for studying the transition between ice giants and gas giants.

Sub-Saturns have no analogs in the solar system, but may shed light on the formation mechanisms of similar intermediate-mass planets in the solar system (Uranus and Neptune). It is commonly assumed that ice giants like Uranus and Neptune formed via core accretion. Under this assumption, the accretion rate must be high enough to ensure that enough gas is accreted, but with high accretion rates, such planets would become gas giants the size of Jupiter and Saturn, instead of ice giants (e.g., Helled & Bodenheimer 2014). To explain the formation of ice giants, core accretion models must prematurely terminate their growth by dispersal of the gaseous disk during envelope contraction (Pollack et al. 1996; Dodson-Robinson & Bodenheimer 2010).

At a period of 11.8 days, HD 89345b is much closer to its host star than the solar system ice giants. Under the core accretion scenario, at such small radial distances, where the solid surface density is high, planets are even more likely to undergo runaway accretion that turns them into gas giants. It would therefore be interesting to see whether the composition of HD 89345b more closely resembles that of ice giants or gas giants. One way to test this is to measure the atmospheric metallicity of the planet through transmission spectroscopy, since the solar system's ice giants have significantly higher

atmospheric metallicities compared to the gas giants (Guillot & Gautier 2014).

During the completion of this paper, we became aware of another paper reporting the discovery of a planet orbiting HD 286123 (Brahm et al. 2018). During the referee process, another paper (Van Eylen et al. 2018) independently reported the discovery of HD 89345b.

Facilities: Kepler, K2, Keck-I (HIRES), Keck-II (NIRC2), Palomar:Hale (PALM-3000/PHARO), FLWO: 1.5m (TRES), APF.

ORCID iDs

Liang Yu https://orcid.org/0000-0003-1667-5427
Joseph E. Rodriguez https://orcid.org/0000-0001-8812-0565
Jason D. Eastman https://orcid.org/0000-0003-3773-5142
Avi Shporer https://orcid.org/0000-0002-1836-3120
B. Scott Gaudi https://orcid.org/0000-0003-0395-9869
Jennifer Burt https://orcid.org/0000-0002-0040-6815
Benjamin J. Fulton https://orcid.org/0000-0003-3504-5316
Evan Sinukoff https://orcid.org/0000-0002-5658-0601
Andrew W. Howard https://orcid.org/0000-0001-8638-0320
Howard Isaacson https://orcid.org/0000-0002-0531-1073
Molly R. Kosiarek https://orcid.org/0000-0002-6115-4359

Joshua E. Schlieder https://orcid.org/0000-0001-5347-7062
Kaloyan Penev https://orcid.org/0000-0003-4464-1371
Andrew Vanderburg https://orcid.org/0000-0001-7246-5438
Keivan G. Stassun https://orcid.org/0000-0002-3481-9052
Allyson Bieryla https://orcid.org/0000-0001-6637-5401
R. Paul Butler https://orcid.org/0000-0003-1305-3761
Michael L. Calkins https://orcid.org/0000-0002-2830-5661
David W. Latham https://orcid.org/0000-0001-9911-7388
Daniel J. Stevens https://orcid.org/0000-0002-5951-8328
Erik A. Petigura https://orcid.org/0000-0003-0967-2893
Laura Kreidberg https://orcid.org/0000-0003-0514-1147

References

Albrecht, S., Winn, J. N., Johnson, J. A., et al. 2012, ApJ, 757, 18
Alibert, Y., Mordasini, C., Benz, W., & Winisdoerffer, C. 2005, A&A, 434, 343
Arras, P., & Socrates, A. 2010, ApJ, 714, 1
Assef, R. J., Gaudi, B. S., & Stanek, K. Z. 2009, ApJ, 701, 1616
Batygin, K., Bodenheimer, P. H., & Laughlin, G. P. 2016, ApJ, 829, 114
Batygin, K., & Stevenson, D. J. 2010, ApJL, 714, L238
Bensby, T., Feltzing, S., & Lundström, I. 2003, A&A, 410, 527
Bodenheimer, P., Hubickyj, O., & Lissauer, J. J. 2000, Icar, 143, 2
Bodenheimer, P., Lin, D. N. C., & Mardling, R. A. 2001, ApJ, 548, 466
Bovy, J. 2017, arXiv:1704.05063
Brahm, R., Espinoza, N., Jordán, A., et al. 2018, arXiv:1802.08865
Buchhave, L. A., Bizzarro, M., Latham, D. W., et al. 2014, Natur, 509, 593
Buchhave, L. A., Bakos, G. Á., Hartman, J. D., et al. 2010, ApJ, 720, 1118
Buchhave, L. A., Latham, D. W., Johansen, A., et al. 2012, Natur, 486, 375
Burrows, A., Guillot, T., Hubbard, W. B., et al. 2000, ApJL, 534, L97
Burrows, A., Hubeny, I., Budaj, J., & Hubbard, W. B. 2007, ApJ, 661, 502
Burrows, A., Marley, M., Hubbard, W. B., et al. 1997, ApJ, 491, 856
Burt, J., Holden, B., Hanson, R., et al. 2015, JATIS, 1, 044003
Butler, R. P., Marcy, G. W., Williams, E., et al. 1996, PASP, 108, 500
Choi, J., Dotter, A., Conroy, C., et al. 2016, ApJ, 823, 102
Coelho, P., Barbuy, B., Meléndez, J., Schiavon, R. P., & Castilho, B. V. 2005, A&A, 443, 735
Coşkunoğlu, B., Ak, S., Bilir, S., et al. 2011, MNRAS, 412, 1237
Crossfield, I. J. M., & Kreidberg, L. 2017, AJ, 154, 261
Crossfield, I. J. M., Petigura, E., Schlieder, J. E., et al. 2015, ApJ, 804, 10
Cutri, R. M. 2014, yCat, 2328, 0
Dai, F., & Winn, J. N. 2017, AJ, 153, 205
Demory, B.-O., & Seager, S. 2011, ApJS, 197, 12
Dodson-Robinson, S. E., & Bodenheimer, P. 2010, Icar, 207, 491
Dong, S., Katz, B., & Socrates, A. 2014, ApJL, 781, L5
Dotter, A. 2016, ApJS, 222, 8
Eastman, J. 2017, EXOFASTv2: Generalized publication-quality exoplanet modeling code, Astrophysics Source Code Library, ascl:1710.003
Eastman, J., Gaudi, B. S., & Agol, E. 2013, PASP, 125, 83
Ehrenreich, D., Bonfils, X., Lovis, C., et al. 2014, A&A, 570, A89
Fabrycky, D., & Tremaine, S. 2007, ApJ, 669, 1298
Fortney, J. J., Marley, M. S., & Barnes, J. W. 2007, ApJ, 659, 1661
Fortney, J. J., Mordasini, C., Nettelmann, N., et al. 2013, ApJ, 775, 80
Fu, G., Deming, D., Knutson, H., et al. 2017, ApJL, 847, L22
Fulton, B., Blunt, S., Petigura, E., et al. 2017, California-Planet-Search/radvel: Version 1.0.4, Zenodo, doi:10.5281/zenodo.1127792
Fulton, B. J., Weiss, L. M., Sinukoff, E., et al. 2015, ApJ, 805, 175
Gaia Collaboration, Brown, A. G. A., Vallenari, A., et al. 2016, A&A, 595, A2
Gaia Collaboration, Brown, A. G. A., Vallenari, A., et al. 2018, arXiv:1804.09365
Grunblatt, S. K., Huber, D., Gaidos, E., et al. 2017, arXiv:1706.05865
Guillot, T., & Gautier, D. 2014, arXiv:1405.3752
Guillot, T., & Showman, A. P. 2002, A&A, 385, 156
Hartman, J. D., Bakos, G. Á., Bhatti, W., et al. 2016, AJ, 152, 182
Hayward, T. L., Brandl, B., Pirger, B., et al. 2001, PASP, 113, 105
Helled, R., & Bodenheimer, P. 2014, ApJ, 789, 69
Hirsch, L. A., Ciardi, D. R., Howard, A. W., et al. 2017, AJ, 153, 117
Høg, E., Fabricius, C., Makarov, V. V., et al. 2000, A&A, 355, L27
Howard, A. W., Johnson, J. A., Marcy, G. W., et al. 2009, ApJ, 696, 75
Howard, A. W., Johnson, J. A., Marcy, G. W., et al. 2010, ApJ, 721, 1467
Howell, S. B., Rowe, J. F., Bryson, S. T., et al. 2012, ApJ, 746, 123
Huber, D., Zinn, J., Bojsen-Hansen, M., et al. 2017, ApJ, 844, 102

Jackson, B., Barnes, R., & Greenberg, R. 2009, ApJ, 698, 1357
Johnson, J. A., Aller, K. M., Howard, A. W., & Crepp, J. R. 2010, PASP, 122, 905
Knutson, H. A., Benneke, B., Deming, D., & Homeier, D. 2014, Natur, 505, 66
Kolbl, R., Marcy, G. W., Isaacson, H., & Howard, A. W. 2015, AJ, 149, 18
Kreidberg, L., Bean, J. L., Désert, J.-M., et al. 2014, Natur, 505, 69
Kreidberg, L., Line, M. R., Thorngren, D., Morley, C. V., & Stevenson, K. B. 2017, arXiv:1709.08635
Kurucz, R. L. 1992, in IAU Symp. 149, The Stellar Populations of Galaxies, ed. B. Barbuy & A. Renzini (Dordrecht: Kluwer), 225
Li, G., & Winn, J. N. 2016, ApJ, 818, 5
Lin, D. N. C., Bodenheimer, P., & Richardson, D. C. 1996, Natur, 380, 606
Lopez, E. D., & Fortney, J. J. 2016, ApJ, 818, 4
Lucy, L. B., & Sweeney, M. A. 1971, AJ, 76, 544
Marcy, G. W., & Butler, R. P. 1992, PASP, 104, 270
Mazeh, T., Perets, H. B., McQuillan, A., & Goldstein, E. S. 2015, ApJ, 801, 3
Miller, N., & Fortney, J. J. 2011, ApJL, 736, L29
Mordasini, C., Mollière, P., Dittkrist, K.-M., Jin, S., & Alibert, Y. 2015, IJAsB, 14, 201
Morley, C. V., Fortney, J. J., Kempton, E. M.-R., et al. 2013, ApJ, 775, 33
Pecaut, M. J., & Mamajek, E. E. 2013, ApJS, 208, 9
Petigura, E. A. 2015, PhD thesis, Univ. California
Petigura, E. A., Howard, A. W., Lopez, E. D., et al. 2016, ApJ, 818, 36
Petigura, E. A., Howard, A. W., & Marcy, G. W. 2013a, PNAS, 110, 19273
Petigura, E. A., Marcy, G. W., & Howard, A. W. 2013b, ApJ, 770, 69

Petrovich, C., & Tremaine, S. 2016, ApJ, 829, 132
Pollack, J. B., Hubickyj, O., Bodenheimer, P., et al. 1996, Icar, 124, 62
Raghavan, D., McAlister, H. A., Henry, T. J., et al. 2010, ApJS, 190, 1
Rasio, F. A., & Ford, E. B. 1996, Sci, 274, 954
Santos, N. C., Israelian, G., & Mayor, M. 2004, A&A, 415, 1153
Schlaufman, K. C. 2010, ApJ, 719, 602
Schlegel, D. J., Finkbeiner, D. P., & Davis, M. 1998, ApJ, 500, 525
Shporer, A., Zhou, G., Fulton, B. J., et al. 2017, AJ, 154, 188
Sinukoff, E., Howard, A. W., Petigura, E. A., et al. 2016, ApJ, 827, 78
Skrutskie, M. F., Cutri, R. M., Stiening, R., et al. 2006, AJ, 131, 1163
Smith, A. M. S., Gandolfi, D., Barragán, O., et al. 2017, MNRAS, 464, 2708
Spiegel, D. S., & Madhusudhan, N. 2012, ApJ, 756, 132
Stevenson, K. B. 2016, ApJL, 817, L16
Szentgyorgyi, A. H., & Furész, G. 2007, RMxAC, 28, 129
Torres, G., Fischer, D. A., Sozzetti, A., et al. 2012, ApJ, 757, 161
Valenti, J. A., Butler, R. P., & Marcy, G. W. 1995, PASP, 107, 966
Van Eylen, V., Dai, F., Mathur, S., et al. 2018, arXiv:1805.01860
Vanderburg, A., & Johnson, J. A. 2014, PASP, 126, 948
Vanderburg, A., Latham, D. W., Buchhave, L. A., et al. 2016, ApJS, 222, 14
Vogt, S. S., Allen, S. L., Bigelow, B. C., et al. 1994, Proc. SPIE, 2198, 362
Vogt, S. S., Radovan, M., Kibrick, R., et al. 2014, PASP, 126, 359
Winn, J. N., Fabrycky, D., Albrecht, S., & Johnson, J. A. 2010, ApJL, 718, L145
Wright, E. L., Eisenhardt, P. R. M., & Mainzer, A. K. 2010, AJ, 140, 1868
Yi, S., Demarque, P., Kim, Y.-C., et al. 2001, ApJS, 136, 417